Article

6-Bromo-2-hydroxypyridinate-bridged Paddlewheel-Type Dirhodium Complex Isomers: Synthesis, Crystal Structures, Electrochemical Properties, and Structure-Dependent Absorption Properties

Kozo Sato, Natsumi Yano [ID] and Yusuke Kataoka *[ID]

Department of Chemistry, Graduate School of Natural Science and Technology, Shimane University, 1060, Nishikawatsu, Matsue 690-8504, Shimane, Japan
* Correspondence: kataoka@riko.shimane-u.ac.jp

Abstract: Two new paddlewheel-type dirhodium (Rh_2) complex isomers, formulated as *trans-2,2*- and *3,1*-forms of $[Rh_2(bhp)_4]$ (bhp = 6-bromo-2-hydroxypyridinate), were obtained by the reaction of 6-bromo-2-hydroxypyridine with $[Rh_2(O_2CCH_3)_4(H_2O)_2]$ and characterized by NMR, ESI-MS, and elemental analyses. Single crystal X-ray diffraction analyses clarified that the crystal structure of *trans-2,2*-form takes a conventional paddlewheel-type dimer structure with no axial coordination ligands, i.e., *trans-2,2*-$[Rh_2(bhp)_4]$, whereas that of the *3,1*-form changed significantly depending on the kinds of solvent used for crystallization processes; dimer-of-dimers-type tetrarhodium complex, i.e., *3,1*-$[Rh_2(bhp)_4]_2$, and a conventional paddlewheel-type dimer complex with an axial DMF ligand, i.e., *3,1*-$[Rh_2(bhp)_4(DMF)]$, were observed. The *3,1*-form showed unique absorption changes that were not observed in the *trans-2,2*-form; the *trans-2,2*-form showed an absorption band at approximately 780 nm both in the solid state and in solution (CH_2Cl_2 and DMF), whereas the *3,1*-form showed a similar absorption band at 783 nm in CH_2Cl_2 solution, but their corresponding bands were blue-shifted in solid state (655 nm) and in DMF solution (608 nm). The molecular structures and the origin of their unique absorption properties of these Rh_2 complexes were investigated using density functional theory (DFT) and time-dependent DFT (TDDFT).

Keywords: dinuclear complexes; rhodium complexes; coordination isomers; crystal structures; electronic structures; absorption properties

1. Introduction

Paddlewheel-type dinuclear complexes with multiple bonds or orbital interactions between two metal atoms have been developed extensively not only because of the interest in their molecular structures, electronic features, and functionalities but also because they are useful building blocks for supramolecular complexes, coordination polymers, and metal-organic frameworks (MOFs) [1–6]. As is well known, this structural motif can be formed using most transition metal ions. Among them, dirhodium(II) (Rh_2^{4+}) complexes [1,7–10], which have a single Rh-Rh bond originating from the $\sigma^2\pi^4\delta^2\delta^{*2}\pi^{*4}$ orbital interactions, are particularly interesting because of their excellent catalytic [11–17], sensing [18,19], and medical functionalities [20]. These functionalities are strongly influenced by the type of bridging ligand coordinated at the equatorial positions of the Rh_2 core. The majority of bridging ligands in Rh_2 complexes are carboxylates, but other bidentate ligands with heterodonor sites, such as amidates [1,10] and amidinates [8], can also be used as bridging ligands for Rh_2 complexes.

2-Hydroxypyridine (hp) derivatives [21–26] are also available as bridging ligands, and homoleptic paddlewheel-type dinuclear complexes with four hp derivative ligands, $[M_2(hp)_4]$, are expected to form four coordination isomers: *4,0*-, *3,1*-, *trans-2,2*-, and *cis-2,2*-form structures (Scheme 1). In this regard, it is known that the introduction of a substituent

at the 6-position of the hp ligand can somewhat control its coordination isomerization. For example, 6-fluoro-2-hydroxypyridinate (fhp)-coordinated Rh$_2$ complex, [Rh$_2$(fhp)$_4$], adopts the *4,0*-form structure as the main product [21,22], whereas 6-chloro-2-hydroxypyridine (chp) or 6-methyl-2-hydroxypyridine (mhp) coordinated Rh$_2$ complexes, i.e., [Rh$_2$(chp)$_4$] or [Rh$_2$(mhp)$_4$], afford *trans-2,2*- and *3,1*-form structures as the main and minor products, respectively [23]. Single crystal X-ray diffraction (SCXRD) studies of 6-substituted hp-bridged Rh$_2$ complexes clarified that the *4,0*- and *3,1*-form structures can coordinate an axial donor ligand at the Rh atom, which is surrounded by four and three O atoms of hp derivatives, respectively, whereas *trans-2,2*-form structure cannot possess donor ligands at the axial positions of the Rh-Rh bond because of the steric hindrance of the substituents [21–24].
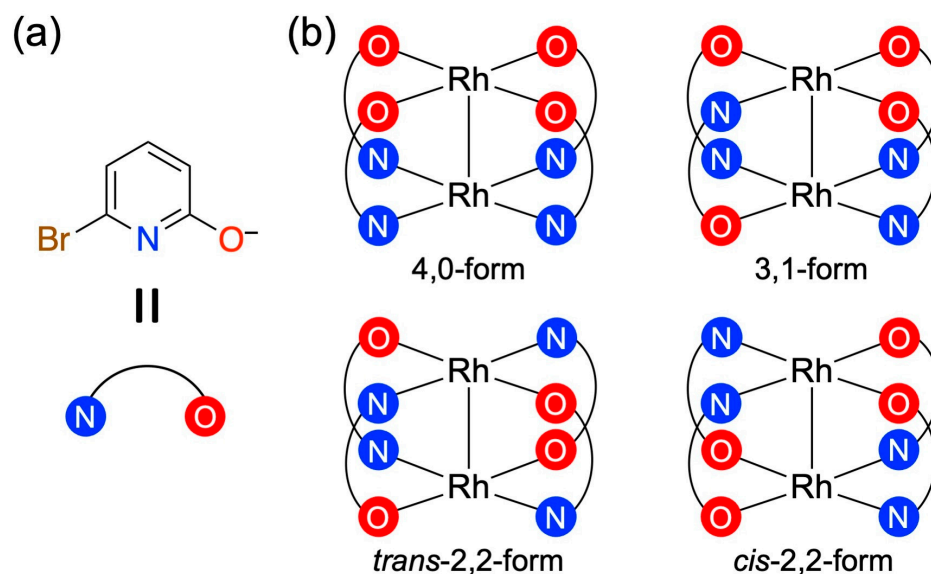
Scheme 1. Molecular structures of (**a**) bhp⁻ ligand and (**b**) coordination isomers of [Rh$_2$(bhp)$_4$].

Although reports on Rh$_2$ complexes coordinated with four hp derivatives or related *N^O*-bridging ligands are still relatively limited, they exhibit excellent catalytic activity in electrochemical and photochemical hydrogen evolution reactions [22], enantioselective S-H and C-H insertion reactions [15,27], and cyclopropanation reactions [28]. Therefore, further development and detailed fundamental studies of Rh$_2$ complexes with hp derivatives are required. Herein, we report the synthesis, characterization, crystal structures, electrochemical properties, and absorption spectral features of paddlewheel-type Rh$_2$ complexes with 6-bromo-2-hydroxypyridinate (bhp). From NMR, ESI-MS, elemental analyses, and SCXRD analyses, it was revealed that two coordination isomers, *trans-2,2*- and *3,1*-forms, can be isolated. Interestingly, the crystal structures of the *3,1*-form change significantly depending on the type of solvent used for the crystallization processes; a dimer-of-dimers-type complex, *3,1*-[Rh$_2$(bhp)$_4$]$_2$, and a dimer complex with an axial DMF ligand, *3,1*-[Rh$_2$(bhp)$_4$(DMF)], were obtained. Moreover, the *3,1*-form exhibited unique absorption spectral changes that were not observed for the *trans-2,2*-form. The molecular structures and the origin of unique absorption properties were also closely investigated by the density-functional theory (DFT) and time-dependent DFT (TDDFT) calculations and were discussed in this study.

2. Results

2.1. Synthesis and Characterizations

The coordination isomers, *trans-2,2*- and *3,1*-forms of [Rh$_2$(bhp)$_4$], were obtained by the reaction of [Rh$_2$(O$_2$CCH$_3$)$_4$(H$_2$O)$_2$] with 10 equivalents of 6-bromo-2-hydroxypyridine in chlorobenzene under N$_2$ atmosphere, followed by column chromatography (silica gel) and drying at 393 K under vacuum. An orange powder of *trans-2,2*-form and a yellowish green powder of *3,1*-form were isolated in 63.6% and 2.5% yields, respectively, indicating

that the coordination structure of *trans-2,2*-form is energetically more stable than that of *3,1*-form. Although some precipitates, including rhodium black, were found in the reaction solution after refluxing, they are insoluble in common solvents and could not be structurally characterized.

The isolated *trans-2,2*- and *3,1*-forms were characterized using ESI-MS, NMR spectroscopy, and elemental analyses. In the ESI-MS spectra of the *trans-2,2*- and *3,1*-forms, intense peaks appeared at 920.5531 and 920.5535 *m/z*, respectively, which correspond to the calculated $[M + Na]^+$ value (920.5555 *m/z*) for the complex of two Rh atoms and four bhp ligands. As shown in Figures S1 and S2, the isotope distributions of the *trans-2,2*- and *3,1*-forms matched well with each other and with the simulation results for $[Rh_2(bhp)_4]$. No other intense peaks were observed in the spectra. Elemental analyses also revealed that the observed CHN ratios of *trans-2,2*- and *3,1*-forms correspond to the calculated ratio of dehydrated $[Rh_2(bhp)_4]$. The ^1H NMR of *trans-2,2*-form showed three doublet of doublet signals at 7.24, 6.78, and 6.35 ppm, with integral ratio of 1:1:1 (Figure S3). This spectral feature is similar to that of *trans-2,2*-$[Rh_2(chp)_4]$ with D_{2h} molecular symmetry [29]. In the $^{13}C\{^1H\}$ NMR spectrum of *trans-2,2*-form, five resonances were observed as well resolved signals in the aromatic region. On the other hand, the proton signals of *3,1*-form were observed in the region of 6.21–7.20 ppm, with integral ratio of 1:1:1:1:1:2:2:3[overlapped signal] (Figure S4). In addition, fifteen resonances were overserved in the $^{13}C\{^1H\}$ NMR spectrum of *3,1*-form. These NMR results are consistent with the *3,1*-arrangement structure with C_{2v} molecular symmetry.

2.2. Single Crystal X-ray Diffraction Analyses

Single crystals of *trans-2,2*-$[Rh_2(bhp)_4]$, *3,1*-$[Rh_2(bhp)_4]_2$, and *3,1*-$[Rh_2(bhp)_4(DMF)]$ suitable for SCXRD analysis were grown using the methods described in the experimental section. Diffraction analyses revealed that *trans-2,2*-$[Rh_2(bhp)_4]$ crystallized in the $P\,2_1/n$ space groups (monoclinic system), whereas *3,1*-$[Rh_2(bhp)_4]_2$ and *3,1*-$[Rh_2(bhp)_4(DMF)]$ crystallized in the *P*-1 (triclinic system) and $P\,2_12_12_1$ space groups (orthorhombic system), respectively. Figure 1 shows the crystal structures with selected numbering schemes of *trans-2,2*-$[Rh_2(bhp)_4]$, *3,1*-$[Rh_2(bhp)_4]_2$, and *3,1*-$[Rh_2(bhp)_4(DMF)]$. Selected bond lengths and angles of their crystal structures are summarized in Tables S1–S3.

As expected, the obtained structures consist of the paddlewheel core and are isomeric. In *trans-2,2*-$[Rh_2(bhp)_4]$, the Rh_2 core is bridged by four bhp ligands with *trans-2,2*-arrangemnet and is not coordinated by solvent molecules as the axial ligands because of the bulky bromide groups, similar to the structures of *trans-2,2*-$[Rh_2(chp)_4]$ and *trans-2,2*-$[Rh_2(mhp)_4]$ [23]. By contrast, the Rh_2 core in *3,1*-$[Rh_2(bhp)_4(DMF)]$ is coordinated by four bhp ligands with *3,1*-arrangement, and the Rh atom surrounded by three oxygen atoms and one nitrogen atom of the bhp ligands is further coordinated by a DMF molecule, which was used as the recrystallization solvent. In the *3,1*-$[Rh_2(bhp)_4]_2$ structure, two *3,1*-$[Rh_2(bhp)_4]$ units self-aggregate with bonds between the oxygen atom of one bhp ligand in *3,1*-$[Rh_2(bhp)_4]$ and the axial position of another Rh_2 unit. Similar "dimer-of-dimers-type" structure was found in the crystal structure of *3,1*-$[Ru_2(chp)_4]_2$ [30]. The averaged Rh_2-O_{axial} bond lengths in *3,1*-$[Rh_2(bhp)_4]_2$ and *3,1*-$[Rh_2(bhp)_4(DMF)]$ are 2.293 and 2.173 Å, respectively, which are sizably longer than the averaged Rh_2-$O_{equatrial}$ bond lengths in *3,1*-$[Rh_2(bhp)_4]_2$ (2.022 Å) and *3,1*-$[Rh_2(bhp)_4(DMF)]$ (2.031 Å). These results indicate that the coordination energies of the Rh-O_{axial} bonds in *3,1*-$[Rh_2(bhp)_4]_2$ and *3,1*-$[Rh_2(bhp)_4(DMF)]$ are considerably weaker than those of the Rh_2-$O_{equatrial}$ bonds. The bhp ligands in *3,1*-$[Rh_2(bhp)_4]_2$ and *3,1*-$[Rh_2(bhp)_4(DMF)]$ are slightly twisted, whereas those in *trans-2,2*-$[Rh_2(bhp)_4]$ are almost planar: averaged dihedral angles of N-Rh-Rh-O in *3,1*-$[Rh_2(bhp)_4]_2$, *3,1*-$[Rh_2(bhp)_4(DMF)]$, and *trans-2,2*-$[Rh_2(bhp)_4]$ are 22.59°, 23.39°, and 1.66°, respectively. Ligand twisting is presumed to be a structural uniqueness of the *3,1*-form, because similar twisted (*3,1*-form) structures were found when mhp or chp were used as the bridging ligands for Rh_2 complexes [23]. The Rh-Rh bond length of *trans-2,2*-$[Rh_2(bhp)_4]$ was determined to be 2.3902(4) Å, which is slightly longer than that of *trans-2,2*-$[Rh_2(chp)_4]$

(2.379(1) Å) and *trans-2,2*-[Rh$_2$(mhp)$_4$] (2.359(1) Å) [23]. This slight increase in the Rh-Rh bond length is presumably due to the electron-withdrawing effects of the bromide groups of the bhp ligands. The Rh-Rh bond length of *3,1*-[Rh$_2$(bhp)$_4$]$_2$ and *3,1*-[Rh$_2$(bhp)$_4$(DMF)] are 2.3704(4) and 2.3726(11) Å, which are slightly (0.02 Å) shorter than those of *trans-2,2*-[Rh$_2$(bhp)$_4$] and *4,0*-[Rh$_2$(fhp)$_4$(DMF)] (2.3970 Å) [22]. The shorter Rh-Rh bond lengths in *3,1*-[Rh$_2$(bhp)$_4$]$_2$ and *3,1*-[Rh$_2$(bhp)$_4$(DMF)] than in *trans-2,2*-[Rh$_2$(bhp)$_4$] may be owing to the axial coordination effect rather than the influence of the structural arrangement.
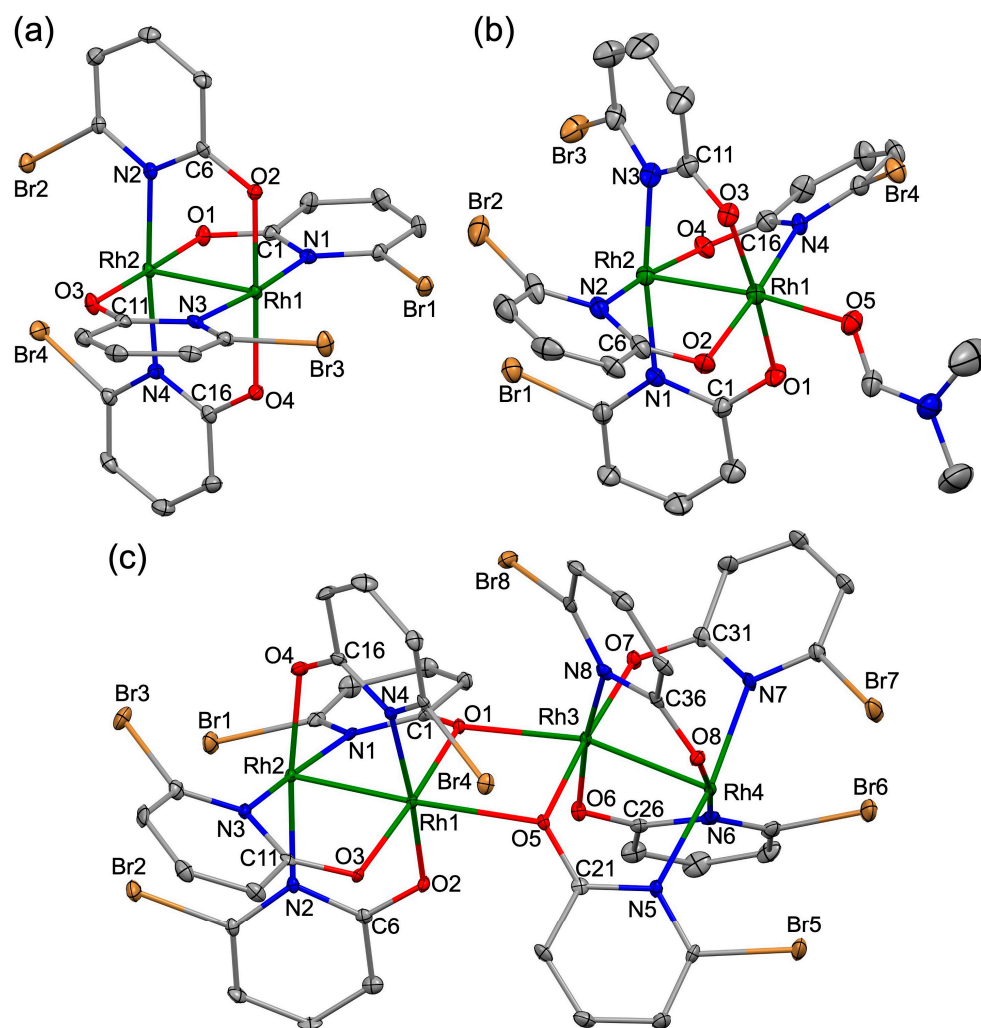

Figure 1. Crystal structures of (**a**) *trans-2,2*-[Rh$_2$(bhp)$_4$], (**b**) *3,1*-[Rh$_2$(bhp)$_4$(DMF)], and (**c**) *3,1*-[Rh$_2$(bhp)$_4$]$_2$. Thermal ellipsoids were drawn at 30% probability. Hydrogen atoms and solvents were omitted for clarity.

2.3. Structural Stabilities and Favorable Spin States

To investigate the structural characteristics of *3,1*-[Rh$_2$(bhp)$_4$], restricted DFT (B3LYP functional) calculations of *3,1*-[Rh$_2$(bhp)$_4$(DMF)] in DMF and *3,1*-[Rh$_2$(bhp)$_4$]$_2$ in the gas phase were computed. The zero-point energy (ZPE) of optimized geometry of *3,1*-[Rh$_2$(bhp)$_4$]$_2$ is 5.67 kcal/mol more stable than the double value of ZPE of optimized geometry of *3,1*-[Rh$_2$(bhp)$_4$]. Moreover, the basis set superposition error (BSSE)-corrected aggregation energy between two *3,1*-[Rh$_2$(bhp)$_4$] fragments in *3,1*-[Rh$_2$(bhp)$_4$]$_2$ was calculated to be −9.69 kcal/mol. These results suggest that the desolvated *3,1*-[Rh$_2$(bhp)$_4$] is more stable in forming a dimer-of-dimers structure than the discrete dimer structure in the solid state. In *3,1*-[Rh$_2$(bhp)$_4$(DMF)], the BSSE-corrected binding energy between *3,1*-[Rh$_2$(bhp)$_4$] and DMF fragments was estimated to be −11.23 kcal/mol, indicating that *3,1*-[Rh$_2$(bhp)$_4$] in DMF solution is more favorable to form the DMF-adducted structure

3,1-[Rh$_2$(bhp)$_4$(DMF)] than the dimer-of-dimers-type structure *3,1*-[Rh$_2$(bhp)$_4$]$_2$. These calculated results are consistent with the experimentally obtained crystal structures.

The frontier molecular orbitals (MOs) of the optimized geometries of *trans-2,2*-[Rh$_2$(bhp)$_4$] and *3,1*-[Rh$_2$(bhp)$_4$] in CH$_2$Cl$_2$, *3,1*-[Rh$_2$(bhp)$_4$(DMF)] in DMF, and *3,1*-[Rh$_2$(bhp)$_4$]$_2$ in the gas phase are shown in Figure 2. In all the complexes, the highest occupied MO (HOMO) and lowest unoccupied MO (LUMO) are mainly localized on the δ*(Rh$_2$)/π(bhp) and σ*(Rh$_2$) orbitals, respectively. The orbital energies of HOMO and LUMO of *trans-2,2*-[Rh$_2$(bhp)$_4$] and *3,1*-[Rh$_2$(bhp)$_4$] are almost identical, between the complexes. The orbital energies of LUMO of *3,1*-[Rh$_2$(bhp)$_4$(DMF)] and *3,1*-[Rh$_2$(bhp)$_4$]$_2$ are more destabilized than that of *3,1*-[Rh$_2$(bhp)$_4$] because of the anti-bonding orbital interaction between the σ*(Rh$_2$) and p(O$_{axial}$) orbitals.
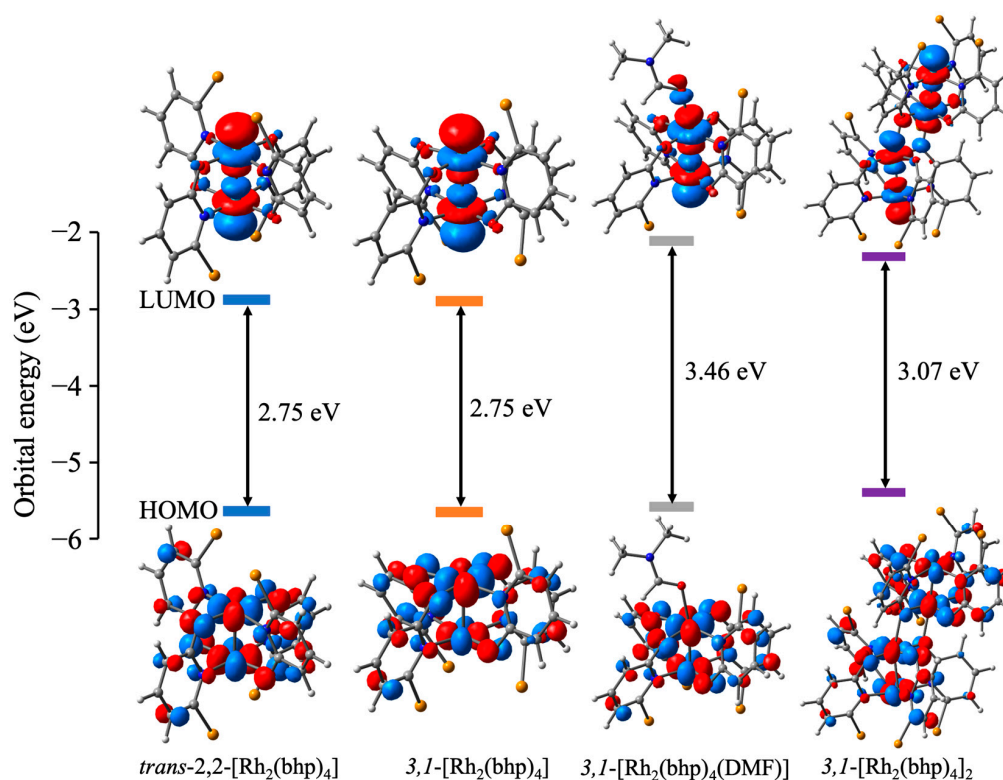

Figure 2. Frontier MOs of *trans*-2,2-[Rh$_2$(bhp)$_4$] and *3,1*-[Rh$_2$(bhp)$_4$] in CH$_2$Cl$_2$, *3,1*-[Rh$_2$(bhp)$_4$(DMF)] in DMF, and *3,1*-[Rh$_2$(bhp)$_4$]$_2$ in the gas phase.

2.4. Electrochemical Properties

Cyclic voltammetry (CV) measurements were performed to investigate the electrochemical properties of *trans-2,2*- and *3,1*-forms of [Rh$_2$(bhp)$_4$] in CH$_2$Cl$_2$ and DMF (see Figure 3). In CH$_2$Cl$_2$, the CV diagram of *trans-2,2*-[Rh$_2$(bhp)$_4$] exhibited two reversible redox waves at E$_{1/2}$ = 1.15 and −1.28 V vs. SCE, whereas that of *3,1*-[Rh$_2$(bhp)$_4$] showed one reversible wave and one irreversible wave at E$_{1/2}$ = 1.07 and −1.17 V vs. SCE, respectively. From the results of the DFT calculations of *trans-2,2*- and *3,1*-forms of [Rh$_2$(bhp)$_4$] in CH$_2$Cl$_2$, the one-electron oxidation and reduction processes could be assigned to occur at the δ*(Rh$_2$)/π(bhp) and σ*(Rh$_2$) orbitals, respectively, which are similar to those of other paddlewheel-type Rh$_2$ complexes [16,31]. Observed E$_{1/2}$ values of *trans-2,2*- and *3,1*-forms of [Rh$_2$(bhp)$_4$] are more positive than those of *trans-2,2*-[Rh$_2$(mhp)$_4$] (E$_{1/2}$ = 0.91 V and −1.36 V vs. Ag/AgCl in CH$_2$Cl$_2$) [29] because of the electron-withdrawing effect of bromide groups in bhp ligands. Similar CV features were also found when DMF was used as the solvent instead of CH$_2$Cl$_2$, whereas observed potentials in DMF were relatively shifted to positive direction than those in CH$_2$Cl$_2$; the E$_{1/2}$ values of *trans-2,2*-[Rh$_2$(bhp)$_4$] in DMF are 1.25 and −1.14 V vs. SCE, whereas those of *3,1*-[Rh$_2$(bhp)$_4$] are 1.13 and −1.12 V vs. SCE.

These results indicate that (i) *3,1*-[Rh$_2$(bhp)$_4$] is more susceptible to one-electron oxidation than *trans-2,2*-[Rh$_2$(bhp)$_4$], and (ii) the one-electron reduction process of *3,1*-[Rh$_2$(bhp)$_4$] is accompanied by structural changes, whereas that of *trans-2,2*-[Rh$_2$(bhp)$_4$] is not.
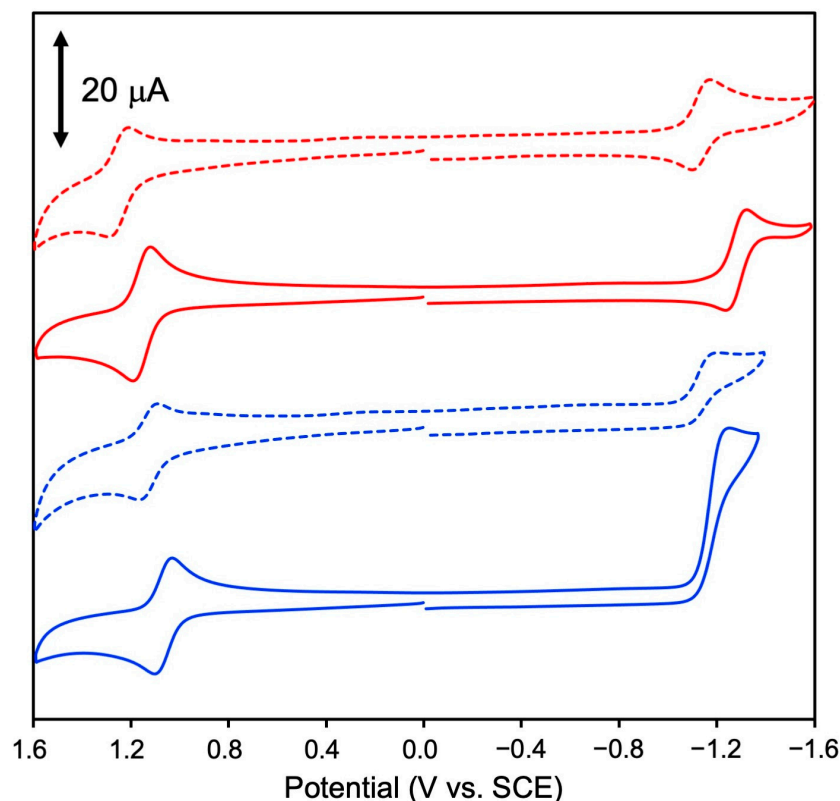
Figure 3. CV diagrams of 0.50 mM *trans-2,2*-[Rh$_2$(bhp)$_4$] (red) and *3,1*-[Rh$_2$(bhp)$_4$] (blue) in CH$_2$Cl$_2$ (solid line) and DMF (dashed line) solutions containing 0.10 M TBAPF$_6$.

2.5. Absorption Properties

The visible absorption spectra in solution (CH$_2$Cl$_2$ and DMF) and diffuse reflectance (DR) spectra in the solid state were measured for *trans-2,2-* and *3,1*-forms of [Rh$_2$(bhp)$_4$]. As shown in Figure 4a, the spectral shape of *trans-2,2*-[Rh$_2$(bhp)$_4$] in CH$_2$Cl$_2$ is nearly identical to that in DMF; an intense "A-band" and a shoulder "B-band" were observed at approximately 780 nm [CH$_2$Cl$_2$: 783 nm (ε = 815). DMF: 780 nm (ε = 816)] and 450–460 nm, respectively. Similar spectral characteristics were also observed in the DR spectrum of *trans-2,2*-[Rh$_2$(bhp)$_4$] (see Figure 4b), although the band maxima of the DR spectrum are slightly blue-shifted compared to those of the absorption spectra. On the other hand, the spectral feature of *3,1*-[Rh$_2$(bhp)$_4$] drastically changed depending on the solvent used; the A-band in CH$_2$Cl$_2$ was observed at 783 nm (ε = 475), similar to *trans-2,2*-[Rh$_2$(bhp)$_4$], whereas that in DMF was observed at 608 nm (ε = 260). The absorption coefficient of the A-band of *3,1*-[Rh$_2$(bhp)$_4$] is relatively lower than that of *trans-2,2*-[Rh$_2$(bhp)$_4$]. The B-band of *3,1*-[Rh$_2$(bhp)$_4$] was observed at approximately 450–460 nm, which is nearly the same as that of *trans-2,2*-[Rh$_2$(bhp)$_4$]. The shape of the DR spectrum of *3,1*-[Rh$_2$(bhp)$_4$], which possesses an A-band at 655 nm and a B-band at 450–460 nm, is apparently different from the shapes of the absorption spectrum of *3,1*-[Rh$_2$(bhp)$_4$] in CH$_2$Cl$_2$ and the DR spectrum of *trans-2,2*-[Rh$_2$(bhp)$_4$], but similar to that of *3,1*-[Rh$_2$(bhp)$_4$] in DMF. The previous literature reports that the A-band of a paddlewheel-type Rh$_2$ complex is blue-shifted when the ligands are coordinated to the axial positions of the Rh$_2$ core [32,33]. Therefore, it is considered that nearly all the as-synthesized *3,1*-[Rh$_2$(bhp)$_4$] in the solid state forms a dimer-of-dimers structure by self-aggregation, as found in the crystal structure of *3,1*-[Rh$_2$(bhp)$_4$]$_2$ but does not form a discrete dimer structure.
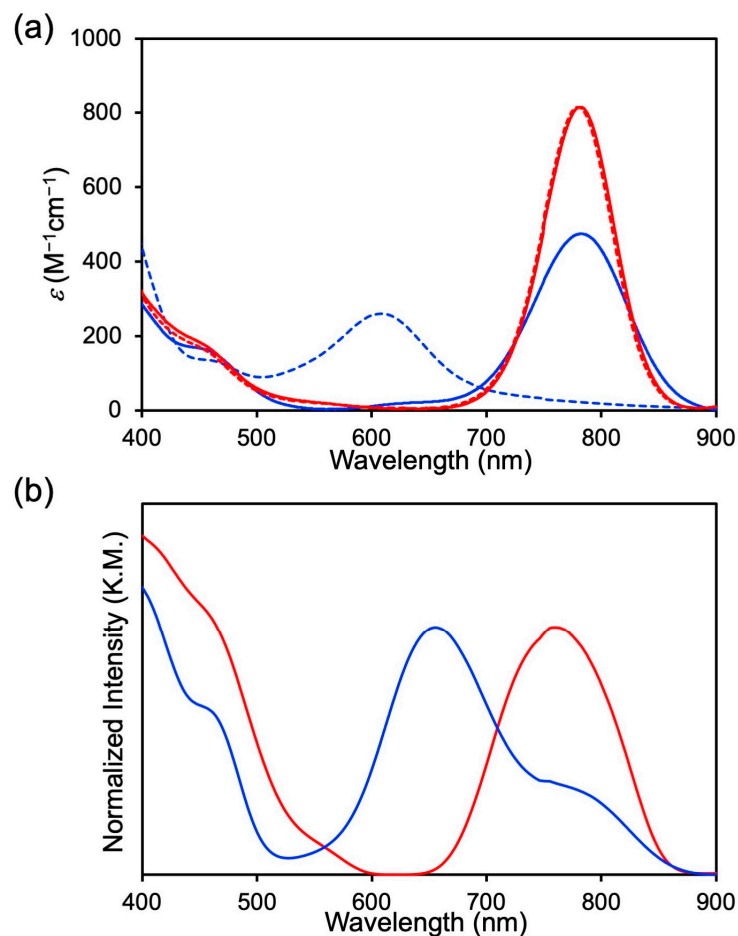
Figure 4. (**a**) Absorption spectra of *trans*-2,2-[Rh$_2$(bhp)$_4$] (red) and *3,1*-[Rh$_2$(bhp)$_4$] (blue) in CH$_2$Cl$_2$ (solid line) and DMF (dashed line), (**b**) DR spectra of *trans*-2,2-[Rh$_2$(bhp)$_4$] (red) and *3,1*-[Rh$_2$(bhp)$_4$] (blue).

To clarify the absorption spectral features of *trans-2,2* and *3,1*-forms of [Rh$_2$(bhp)$_4$], TDDFT calculations of *trans-2,2*-[Rh$_2$(bhp)$_4$] and *3,1*-[Rh$_2$(bhp)$_4$] in CH$_2$Cl$_2$, *3,1*-[Rh$_2$(bhp)$_4$-(DMF)] in DMF, and *3,1*-[Rh$_2$(bhp)$_4$]$_2$ in the gas phase were performed. The computed results, such as the excitation wavelengths, oscillator strengths, and dominant excitation characters are summarized in Tables S5–S7. The simulated excitation wavelengths of the complexes generally reproduced the observed absorption wavelengths. That is, the simulated excitation wavelengths of the A-bands of *3,1*-[Rh$_2$(bhp)$_4$(DMF)] in DMF and *3,1*-[Rh$_2$(bhp)$_4$]$_2$ were blue-shifted with respect to that of *3,1*-[Rh$_2$(bhp)$_4$] in CH$_2$Cl$_2$, similarly to their observed spectra. The excitation characters of A-band of *trans-2,2*-[Rh$_2$(bhp)$_4$] and *3,1*-[Rh$_2$(bhp)$_4$] in CH$_2$Cl$_2$ possess the π^*(Rh$_2$)→σ^*(Rh$_2$) excitations as the dominant characters, whereas those of *3,1*-[Rh$_2$(bhp)$_4$(DMF)] and *3,1*-[Rh$_2$(bhp)$_4$]$_2$ comprise π^*(Rh$_2$)→σ^*(Rh$_2$) excitations as the dominant characters with δ^*(Rh$_2$)→σ^*(Rh$_2$) excitations as the minor contribution. These results indicated that the main characteristics of A-band of *3,1*-[Rh$_2$(bhp)$_4$], *3,1*-[Rh$_2$(bhp)$_4$(DMF)], and *3,1*-[Rh$_2$(bhp)$_4$]$_2$ are commonly d(Rh$_2$)→σ^*(Rh$_2$) excitation characters. That is, it was clarified that the reason why the absorption wavelengths of the A-band of *3,1*-[Rh$_2$(bhp)$_4$(DMF)] and *3,1*-[Rh$_2$(bhp)$_4$]$_2$ were found at shorter wavelengths than that of *3,1*-[Rh$_2$(bhp)$_4$] is owing to the stabilization and destabilization of the orbital energies of σ^*(Rh$_2$), which are obviously changed by the axial coordination of *O*-donor molecules.

3. Materials and Methods

3.1. Chemicals and Instruments

6-bromo-2hydroxypyridine was purchased from Tokyo Chemical Industries (Tokyo, Japan), and organic solvents were obtained from Wako Pure Chemical Industries (Osaka, Japan) and used as received without further purification. $[Rh_2(O_2CCH_3)_4(H_2O)_2]$ was synthesized according to methods described in the literatures [34]. Electrospray ionization mass spectroscopy (ESI-MS) were performed with a Bruker micrOTOF-II instrument (Bruker, Billerica, MA, USA) in the positive-ion mode. Nuclear magnetic resonance spectra (NMR) were recorded on a JEOL JNM-ECX500 spectrometer (JEOL, Tokyo, Japan) operating at 500 MHz for ^{1}H and 126 MHz for ^{13}C in a DMSO-d_6. Chemical shifts are referenced to the residual DMSO signal. Elemental analyses were performed with a YANACO CHN corder MT-6 instrument (Yanaco, Tokyo, Japan). Absorption spectra were measured with a JASCO V-670 spectrophotometer (JASCO, Tokyo, Japan). Diffuse reflectance (DR) spectra were acquired using a JASCO V-670 spectrophotometer equipped with an ISN-923 integrating sphere (JASCO, Tokyo, Japan). Cyclic voltammetry (CV) measurements of the $[Rh_2(bhp)_4]$ (0.50 mM) in dried DMF and CH_2Cl_2 solutions containing 0.10 M TBAPF$_6$ were performed using a HOKUTO DENKO HZ-7000 HAG1232m system (Meiden Hokuto Coorporation, Tokyo, Japan) at a scan rate of 100 mV/s. The glassy carbon, platinum wire, and saturated calomel electrode were employed as the working, counter, and reference electrodes, respectively.

3.2. Synthesis of trans-2,2-form and 3,1-Form of [Rh₂(bhp)₄]

A mixture of $[Rh_2(O_2CCH_3)_4(H_2O)_2]$ (95.6 mg, 0.20 mmol) and 6-bromo-2-hydroxypyridine (348.0 mg, 2.0 mmol) in 15.0 mL chlorobenzene was refluxed under nitrogen atmosphere for 24 h. After cooled to room temperature, the reaction solution was filtered, and the filtrate was then evaporated under reduced pressure. Obtained residue was separated by a silica-gel column chromatography (eluent: CH_2Cl_2/MeCN/EtOH = 17:2:1 *v/v/v*). The first and second fractions were evaporated to dryness, dried at 393 K under reduced pressure, and obtained as an orange powder (*trans-2,2*-form: 114.2 mg, 63.6%) and a yellowish green powder (*3,1*-form: 4.4 mg, 2.5%), respectively.

Analysis data for *trans-2,2*-form. ^{1}H NMR (500 MHz, DMSO-d_6, δ): 7.24 (dd, *J* = 8.6, 7.5 Hz, 4H), 6.78 (dd, *J* = 7.3, 0.8 Hz, 4H), 6.35 (dd, *J* = 8.6, 1.0 Hz, 4H) ppm. ^{13}C{^{1}H} NMR (126 MHz, DMSO-d_6) δ = 177.87, 139.68, 138.88, 114.87, 114.25 ppm. ESI-MS calcd for $C_{20}H_{12}Br_4N_4O_4Rh_2Na$ [M + Na]$^+$: 920.5555 *m/z*; found 920.5531 *m/z*. EA calcd (%) for $C_{20}H_{12}Br_4N_4O_4Rh_2$: C 26.76, H 1.35, N 6.24; found C 26.76, H 1.51, N 6.34.

Analysis data for *3,1*-form. ^{1}H NMR (500 MHz, DMSO-d_6, δ): 7.20 (m, 3H), 7.08 (dd, *J* = 8.6, 7.1 Hz, 1H), 6.78 (dd, *J* = 7.3, 0.8 Hz, 2H), 6.75 (dd, *J* = 7.3, 1.2 Hz, 1H), 6.58 (dd, *J* = 6.9, 1.2 Hz, 1H), 6.38 (dd, *J* = 8.6, 1.0 Hz, 1H), 6.30 (dd, *J* = 8.4, 0.8 Hz, 2H), 6.21 (dd, *J* = 8.8, 1.1 Hz, 1H) ppm. ^{13}C{^{1}H} NMR (126 MHz, DMSO-d_6, δ): 180.08, 179.39, 179.35, 140.95, 140.10, 140.03, 139.20, 139.11, 139.02, 117.00, 116.36, 115.63, 114.55, 114.20, 113.99 ppm. ESI-MS calcd for $C_{20}H_{12}Br_4N_4O_4Rh_2Na$ [M + Na]$^+$: 920.5555 *m/z*; found 920.5535 *m/z*. EA calcd (%) for $C_{20}H_{12}Br_4N_4O_4Rh_2$: C 26.76, H 1.35, N 6.24; found C 26.69, H 1.46, N 6.11.

3.3. Crystallography

Single crystals of *trans-2,2*-$[Rh_2(bhp)_4]$ suitable for X-ray diffraction were obtained by slow diffusion of hexane into CH_2Cl_2 solution containing *trans-2,2*-form, whereas those of *3,1*-$[Rh_2(bhp)_4]_2$ and *3,1*-$[Rh_2(bhp)_4(DMF)]$ were grown by slow diffusion of diethyl ether into CH_2Cl_2 solution containing *3,1*-form and slow evaporation of DMF solution containing *3,1*-form, respectively. Obtained single crystals were carefully mounted on a MiteGen micromount using a paratone-N oil and then were quickly transferred to the cold nitrogen-steam for data collection. X-ray diffraction data of *trans-2,2*-$[Rh_2(bhp)_4]$ and *3,1*-$[Rh_2(bhp)_4(DMF)]$ were collected on a Rigaku HyPix-6000 detector system (Tokyo, Japan) with a graphite-monochromated Mo *K*α radiation (λ = 0.71073 Å) at 150 K, whereas that of *3,1*-$[Rh_2(bhp)_4]_2$ was collected on a Rigaku Mercury CCD detector system (Tokyo, Japan)

with a graphite-monochromated Mo *K*α radiation (λ = 0.71073 Å) at 150 K. Data processing were performed with CrysAlisPro software (version 1.171.42.49) [35]. The structures were initially solved with SHELXT-2018 program [36] and were then refined with full-matrix least square on F^2 using SHELXL program [37] in the Olex 2 software (version 1.5) [38]. All non-hydrogen atoms were refined using anisotropic displacement parameters, whereas hydrogen atoms were placed in calculated positions and refined as riding model. In the refinement of *trans-2,2*-[Rh$_2$(bhp)$_4$], the residual electron density of disorder solvents was removed by using the solvent mask routine of the Olex 2. Crystallographic data of final refined structures are summarized in Table 1. These crystallographic data can be obtained free of charge from Cambridge Crystallographic Data Centre (CCDC); deposition numbers of *trans-2,2*-[Rh$_2$(bhp)$_4$], *3,1*-[Rh$_2$(bhp)$_4$]$_2$, and *3,1*-[Rh$_2$(bhp)$_4$(DMF)] are CCDC-2328797, 2328798, and 2328799, respectively.

Table 1. Crystallographic data of *trans-2,2*-[Rh$_2$(bhp)$_4$], *3,1*-[Rh$_2$(bhp)$_4$]$_2$, and *3,1*-[Rh$_2$(bhp)$_4$(DMF)].

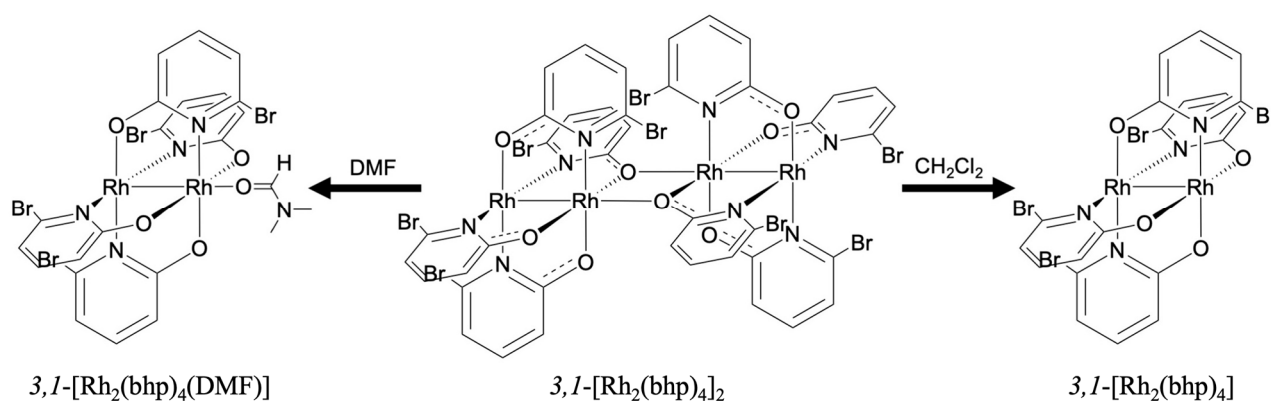|	**trans-2,2-[Rh$_2$(bhp)$_4$]**	**3,1-[Rh$_2$(bhp)$_4$]$_2$**	**3,1-[Rh$_2$(bhp)$_4$(DMF)]**
Chemical formula	C$_{20}$H$_{12}$Br$_4$N$_4$O$_4$Rh$_2$	C$_{42}$H$_{28}$Br$_8$Cl$_4$N$_8$O$_8$Rh$_4$	C$_{23}$H$_{19}$Br$_4$N$_5$O$_5$Rh$_2$
Formula weight	897.80	1965.44	970.89
Crystal system	monoclinic	triclinic	orthorhombic
Space group	*P* 2$_1$/*n*	*P*-1	*P* 2$_1$2$_1$2$_1$
a (Å)	10.7274(3)	11.7389(3)	9.7976(4)
b (Å)	15.1958(4)	14.1558(4)	12.1892(6)
c (Å)	15.1861(4)	18.6200(4)	23.3582(10)
α (deg)	90	109.831(2)	90
β (deg)	103.275(3)	94.751(2)	90
γ (deg)	90	109.617(2)	90
V (Å^3)	2409.36(12)	2673.30(13)	2789.6(2)
Z	4	2	4
D_{calc} (g cm^{-3})	2.475	2.442	2.312
μ (mm^{-1})	8.040	7.471	6.957
F(000)	1688.0	1856	1848.0
R_1 (*I* > 2σ(*I*))	0.0374	0.0319	0.0465
wR_2 (*I* > 2σ(*I*))	0.0879	0.0667	0.1007
R_1 (all data)	0.0443	0.0465	0.0608
wR_2 (all data)	0.0904	0.0716	0.1055
GOF on F^2	1.069	1.013	1.064

3.4. Calculation Details

DFT calculations were performed using the hybrid B3LYP functional [39] with SDD for Rh atoms, aug-cc-pVDZ for N and O atoms, and cc-pVDZ for other atoms by using the Gaussian 16 version C.02 program package [40]. Molecular structures were fully optimized without any symmetry constraints and were then checked by frequency analyses. The polarizable continuum models (PCM) were employed to take account of the solvent effects for the calculations of geometry optimizations, frequency analyses, and MO analyses of *3,1*-[Rh$_2$(bhp)$_4$(DMF)] (ε = 37.219 for DMF) and *trans-2,2*- and *3,1*-forms of [Rh$_2$(bhp)$_4$] (ε = 8.93 for CH$_2$Cl$_2$). The aggregation energy and binding energy were estimated with counterpoise method for removing the basis set superposition error (BSSE). Vertical singlet excitation energies, oscillator strengths (*f*), and assignments of excitation characters were computed with a time-dependent DFT (TDDFT).

4. Conclusions

In this study, two paddlewheel-type Rh$_2$ complex isomers coordinated with bhp ligands, *trans-2,2*- and *3,1*-forms of [Rh$_2$(bhp)$_4$], were successfully prepared and characterized. SCXRD analyses revealed that crystal structure of *3,1*-form changed significantly depending on the kinds of solvent used for crystallization processes; dimer-of-dimers-type tetrarhodium complex, i.e., *3,1*-[Rh$_2$(bhp)$_4$]$_2$, and a conventional paddlewheel-type dimer

complex with an axial DMF ligand, i.e., *3,1*-[Rh$_2$(bhp)$_4$(DMF)], are observed, whereas that of *trans-2,2*-form takes a conventional paddlewheel-type dimer structure with no axial coordination ligands. DFT calculations revealed that *3,1*-[Rh$_2$(bhp)$_4$] prefers to be coordinated by DMF solvent or to form the self-aggregated dimer-of-dimers structure rather than the formation of discrete structure with no axial coordination ligand in the solid state. We confirmed that there were no significant differences in the absorption features of *trans-2,2*-[Rh$_2$(bhp)$_4$] in solution (CH$_2$Cl$_2$ and DMF) and solid states. By contrast, spectral feature of *3,1*-[Rh$_2$(bhp)$_4$] drastically changes; the A-band in CH$_2$Cl$_2$ was observed at 783 nm, whereas those in DMF and in solid state were observed at 608 nm and 655 nm, respectively. TDDFT calculations clarified that this spectral difference is caused by the changes in the coordination environments as illustrated in Scheme 2.

3,1-[Rh$_2$(bhp)$_4$(DMF)]   *3,1*-[Rh$_2$(bhp)$_4$]$_2$ *3,1*-[Rh$_2$(bhp)$_4$]

Scheme 2. Structural changes of *3,1*-[Rh$_2$(bhp)$_4$]$_2$ in DMF and CH$_2$Cl$_2$.

Supplementary Materials: The following supporting information can be downloaded at: https://www.mdpi.com/article/10.3390/inorganics12030070/s1, Figure S1: Observed and simulated ESI-MS spectra of *trans-2,2*-[Rh$_2$(bhp)$_4$]; Figure S2: Observed and simulated ESI-MS spectra of *3,1*-[Rh$_2$(bhp)$_4$]; Figure S3: ^{1}H NMR spectrum of *trans-2,2*-[Rh$_2$(bhp)$_4$] in DMSO-d_6; Figure S4: ^{1}H NMR spectrum of *3,1*-[Rh$_2$(bhp)$_4$] in DMSO-d_6; Table S1: Selected bond lengths (Å) and angles (°) of *trans-2,2*-[Rh$_2$(bhp)$_4$]; Table S2: Selected bond lengths (Å) and angles (°) of *3,1*-[Rh$_2$(bhp)$_4$(DMF)]; Table S3: Selected bond lengths (Å) and angles (°) of *3,1*-[Rh$_2$(bhp)$_4$]$_2$; Table S4: Averaged bond lengths (Å) of optimized geometries of [Rh$_2$(bhp)$_4$] isomers; Table S5: TDDFT results of *trans-2,2*-[Rh$_2$(bhp)$_4$] in CH$_2$Cl$_2$; Table S6: TDDFT results of *3,1*-[Rh$_2$(bhp)$_4$] in CH$_2$Cl$_2$; Table S7: TDDFT results of *3,1*-[Rh$_2$(bhp)$_4$] in DMF; Table S8: TDDFT results of *3,1*-[Rh$_2$(bhp)$_4$] in gas phase.

Data Availability Statement: Crystallographic data of *trans-2,2*-[Rh$_2$(bhp)$_4$], *3,1*-[Rh$_2$(bhp)$_4$(DMF)], and *3,1*-[Rh$_2$(bhp)$_4$]$_2$ can be obtained free of charge from Cambridge Crystallographic Data Centre (CCDC); deposition numbers of *trans-2,2*-[Rh$_2$(bhp)$_4$], *3,1*-[Rh$_2$(bhp)$_4$(DMF)], and *3,1*-[Rh$_2$(bhp)$_4$]$_2$ are CCDC-2328797, 2328798, and 2328799, respectively.

Conflicts of Interest: The authors declare no conflicts of interest.

References

1. Cotton, F.A.; Murillo, C.A.; Walton, R.A. *Multiple Bonds between Metal Atoms*, 3rd ed.; Springer Science and Business Media: New York, NY, USA, 2005.
2. Köberl, M.; Cokoja, M.; Herrmann, W.A.; Kühn, F.E. From molecules to materials: Molecular paddle-wheel synthons of macromolecules, cage compounds and metal–organic frameworks. *Dalton Trans.* **2011**, *40*, 6834–6859. [CrossRef] [PubMed]
3. Chisholm, M.H.; Patmore, N.J. Studies of electronic coupling and mixed valency in metal-metal quadruply bonded complexes linked by dicarboxylate and closely related ligands. *Acc. Chem. Res.* **2007**, *40*, 19–27. [CrossRef] [PubMed]
4. Cotton, F.A.; Lin, C.; Murillo, C.A. Supramolecular arrays based on dimetal building units. *Acc. Chem. Res.* **2001**, *34*, 759–771. [CrossRef] [PubMed]
5. Chui, S.S.Y.; Lo, S.M.F.; Charmant, J.P.H.; Orpen, A.G.; Williams, I.D. A chemically functionalizable nanoporous material [Cu3(TMA)2(H2O)3]n. *Science* **1999**, *283*, 1148–1150. [CrossRef]
6. Eddaoudi, M.; Kim, J.; Wachter, J.B.; Chae, H.K.; O'Keeffe, M.; Yaghi, O.M. Porous Metal-Organic Polyhedra: 25 Å Cuboctahedron Constructed from 12 Cu2(CO2)4 Paddle-Wheel Building Blocks. *J. Am. Chem. Soc.* **2001**, *123*, 4368–4369. [CrossRef] [PubMed]
7. Kataoka, Y.; Yano, N.; Mikuriya, M.; Handa, M. Coordination polymers and metal–organic frameworks based on paddlewheel-type dirhodium(II) tetracarboxylates. *Coord. Chem. Rev.* **2022**, *472*, 214796. [CrossRef]
8. Kataoka, Y.; Yano, N.; Mikuriya, M.; Handa, M. Paddlewheel-type dirhodium complexes with N,N′-bridging ligands. *Coord. Chem. Rev.* **2023**, *479*, 214997. [CrossRef]
9. Berry, J.F. *Metal-Metal Bonded Compounds of the Group IX Elements, Comprehensive Coordination Chemistry III*, 3rd ed.; Constable, E.C., Parkin, G., Que, L., Jr., Eds.; Elsevier: Amsterdam, The Netherlands, 2021; Volume 6, pp. 4–42.
10. Hrdina, R. Dirhodium(II,II) Paddlewheel Complexes. *Eur. J. Inorg. Chem.* **2021**, *6*, 501–528. [CrossRef]
11. Hansen, J.; Davies, H.M.L. High Symmetry Dirhodium(II) Paddlewheel Complexes as Chiral Catalysts. *Coord. Chem. Rev.* **2008**, *252*, 545–555. [CrossRef]
12. Du Bois, J. Rhodium-Catalyzed C–H Amination. An Enabling Method for Chemical Synthesis. *Org. Process Res. Dev.* **2011**, *15*, 758–762. [CrossRef]
13. Fiori, K.W.; Du Bois, J. Catalytic Intermolecular Amination of C–H Bonds: Method Development and Mechanistic Insights. *J. Am. Chem. Soc.* **2007**, *129*, 562–568. [CrossRef]
14. DeAngelis, A.; Panish, R.; Fox, J.M. Rh-Catalyzed Intermolecular Reactions of α-Alkyl-α-Diazo Carbonyl Compounds with Selectivity over β-Hydride Migration. *Acc. Chem. Res.* **2016**, *49*, 115–127. [CrossRef]
15. Zalatan, D.N.; Du Bois, J. A chiral rhodium carboxamidate catalyst for enantioselective C-H amination. *J. Am. Chem. Soc.* **2008**, *130*, 9220–9221. [CrossRef]
16. Kataoka, Y.; Yano, N.; Handa, M.; Kawamoto, T. Intrinsic Hydrogen Evolution Capability and Theoretically Supported Reaction Mechanism of Paddlewheel-type Dirhodium Complex. *Dalton Trans.* **2019**, *48*, 7302–7312. [CrossRef] [PubMed]
17. Kataoka, Y.; Yano, N.; Kohara, Y.; Tsuji, T.; Inoue, S.; Kawamoto, T. Experimental and Theoretical Study of Photochemical Hydrogen Evolution Catalyzed by Paddlewheel-Type Dirhodium Complexes with Electron Withdrawing Carboxylate Ligands. *ChemCatChem* **2019**, *11*, 6218–6226. [CrossRef]
18. Esteban, J.; Ros-Lis, J.V.; Martínez-Máñez, R.; Marcos, M.D.; Moragues, M.; Soto, J.; Sancenón, F. Sensitive and Selective Chromogenic Sensing of Carbon Monoxide by Using Binuclear Rhodium Complexes. *Angew. Chem. Int. Ed.* **2010**, *49*, 4934–4937. [CrossRef] [PubMed]
19. Kataoka, Y.; Kohara, Y.; Yano, N.; Kawamoto, T. Unique vapochromism of a paddlewheel-type dirhodium complex accompanied by dynamic structural and phase transitions. *Dalton Trans.* **2020**, *49*, 14373–14377. [CrossRef]
20. Chifotides, H.T.; Dunber, K.R. Interactions of Metal-Metal-Bonded Antitumor Active Complexes with DNA Fragments and DNA. *Acc. Chem. Res.* **2005**, *38*, 146–156. [CrossRef]
21. Cotton, F.A.; Han, S.; Wang, W. Preparation, Structure, and Properties of the Polar Dirhodium(II) Tetrakis(6-fluoro-2-oxypyridinate) Molecule. *Inorg. Chem.* **1984**, *23*, 4762–4765. [CrossRef]
22. Kataoka, Y.; Sato, K.; Yano, N. Hydroxypyridinate-bridged paddlewheel-type dirhodium complex as a catalyst for photochemical and electrochemical hydrogen evolution. *J. Chem. Phys.* **2023**, *159*, 204304. [CrossRef] [PubMed]
23. Cotton, F.A.; Felthouse, T.R. Seven Dinuclear Rhodium(II) Complexes with o-Oxypyridine Anions as Ligands. *Inorg. Chem.* **1981**, *20*, 584–600. [CrossRef]
24. Clegg, W.; Garner, C.D.; Akhter, L.; Al-Samman, M.H. Steric and Crystal-Packing Effects on the Molecular Structures of Dimetal(II) Tetrakis(2-oxvpyridine) Complexes. *Inorg. Chem.* **1983**, *22*, 2466–2468. [CrossRef]
25. Kawamura, T.; Ebihara, M.; Miyamoto, M. A Three-Dimensional Interaction Network of δ(M-M) and π(ligand) Electrons. The Crystal Structure of [Rh2(mhp)4](SbCl6)·2CH2ClCH2Cl (mhp = 2-oxy-6-methylpyridine). *Chem. Lett.* **1993**, *22*, 1509–1512. [CrossRef]
26. Kawamura, T.; Kachi, H.; Fujii, H.; Kachi-Terajima, C.; Kawamura, Y.; Kanematsu, N.; Ebihara, M.; Sugimoto, K.; Kuroda-Sowa, T.; Munakata, M. δ*MM-πL odd electron delocalization onto aromatic bridging ligands in a paramagnetic dirhodium complex and intermolecular π-stack interaction in crystal. *Bull. Chem. Soc. Jpn.* **2000**, *73*, 657–668. [CrossRef]
27. Brunner, H.; Wutz, K.; Doyle, M.P. Asymmetrische Katalysen, 58. Mitt.: Enantioselektive S-H-und C-H-Insertionen mit optisch aktiven Rh (II)-und Cu (II)-Katalysatoren. *Monatshefte Chem./Chem. Mon.* **1990**, *121*, 755–764. [CrossRef]

28. Doyle, M.P.; Davies, S.B.; Hu, W. Optimization of enantiocontrol in cis-selective cyclopropanation reactions catalyzed by dirhodium (II) tetrakis [alkyl 2-oxaazetidine-4 (S)-carboxylates]. *Chem. Commun.* **2000**, *10*, 867–868. [CrossRef]

29. Li, Z.; David, A.; Albani, B.A.; Pellois, J.P.; Turro, C.; Dunbar, K.R. Optimizing the electronic properties of photoactive anticancer oxypyridine-bridged dirhodium (II, II) complexes. *J. Am. Chem. Soc.* **2014**, *136*, 17058–17070. [CrossRef]

30. Cotton, F.A.; Ren, T.; Eglin, J.L. Preparative, structural, and magnetic studies of 2-hydroxypyridinate complexes of diruthenium (II). *J. Am. Chem. Soc.* **1990**, *112*, 3439–3445. [CrossRef]

31. Ren, T.; Lin, C.; Valente, E.J.; Zubkowski, J.D. The influence of remote substituent in tetrakis(μ-N,N′-diarylformamidinato)-dirhodium(II) compounds. Part 7. Linear free energy relationships in dinuclear compounds. *Inorg. Chim. Acta* **2000**, *297*, 283–290. [CrossRef]

32. Cotton, F.A.; Hillard, E.A.; Murillo, C.A. The first dirhodium tetracarboxylate molecule without axial ligation: New insight into the electronic structures of molecules with importance in catalysis and other reactions. *J. Am. Chem. Soc.* **2002**, *124*, 5658–5660. [CrossRef] [PubMed]

33. Cotton, F.A.; Hillard, E.A.; Liu, C.Y.; Murillo, C.A.; Wang, W.; Wang, X. Steps on the way to the first dirhodium tetracarboxylate with no axial ligation: Synthetic lessons and a plethora of Rh2(O2CR)4L2− n compounds, n = 0, 1, 2. *Inorg. Chim. Acta* **2002**, *337*, 233–246. [CrossRef]

34. Legzdins, P.; Mitchell, R.W.; Rempel, G.L.; Ruddick, J.D.; Wilkinsin, G. The protonation of ruthenium- and rhodium-bridged carboxylates and their use as homogeneous hydrogenation catalysts for unsaturated substances. *J. Chem. Soc. A* **1970**, 3322–3326. [CrossRef]

35. *CrysAlisPro Software System, Rigaku Oxford Diffraction*; Rigaku Corporation: Tokyo, Japan, 2018.

36. Sheldrick, G.M. SHELXT—Integrated space-group and crystal-structure determination. *Acta Cryst.* **2015**, *A71*, 3–8. [CrossRef]

37. Sheldrick, G.M. Crystal structure refinement with SHELXL. *Acta Cryst.* **2015**, *C71*, 3–8.

38. Dolomanov, O.V.; Bourhis, L.J.; Gildea, R.J.; Howard, J.A.K.; Puschmann, H. OLEX2: A complete structure solution, refinement and analysis program. *J. Appl. Cryst.* **2009**, *42*, 339–341. [CrossRef]

39. Becke, A.D. Density-functional thermochemistry. III. The role of exact exchange. *J. Chem. Phys.* **1993**, *98*, 5648–5652. [CrossRef]

40. Frisch, M.J.; Trucks, G.W.; Schlegel, H.B.; Scuseria, G.E.; Robb, M.A.; Cheeseman, J.R.; Scalmani, G.; Barone, V.; Petersson, G.A.; Nakatsuji, H.; et al. *Gaussian 16*; Revision C.01; Gaussian, Inc.: Wallingford, CT, USA, 2016.